Letter

Nano-Ceramic Cathodes via Co-sputtering of Gd−Ce Alloy and Lanthanum Strontium Cobaltite for Low-Temperature Thin-Film Solid Oxide Fuel Cells

Haowen Ren, Yoon Ho Lee, Erik A. Wu, Hyeseung Chung, Ying Shirley Meng, Eric E. Fullerton, and Nguyen Q. Minh*

Cite This: https://dx.doi.org/10.1021/acsaem.0c01147

Read Online

ACCESS | Metrics & More | Article Recommendations | SI Supporting Information

ABSTRACT: We report the electrochemical performance and structural characteristics of porous nanostructured ceramic cathodes for thin-film solid oxide fuel cells (TF-SOFCs) based on yttria-stabilized zirconia (YSZ) electrolytes. The nanostructured cathode is obtained through magnetron co-sputtering of gadolinium−cerium (Gd−Ce) alloy and lanthanum strontium cobaltite perovskite targets. The resultant nanostructure and composition of the ceramic cathode are controlled by adjusting the co-sputtering conditions. The peak power densities in our fabricated TF-SOFCs are the highest reported values for YSZ-based electrolyte SOFCs, showing 0.14, 0.48, 1.21, 2.56, and 3.01 W/cm^2 at 450, 500, 550, 600, and 650 °C, respectively, operating under air and pure hydrogen fuel. The results show that the porosity and composition of the cathode greatly affect the resulting peak power densities. This work illustrates the capability of sputtering to produce stable, scalable, nano-ceramic cathodes with superb peak power densities when integrated in TF-SOFCs.
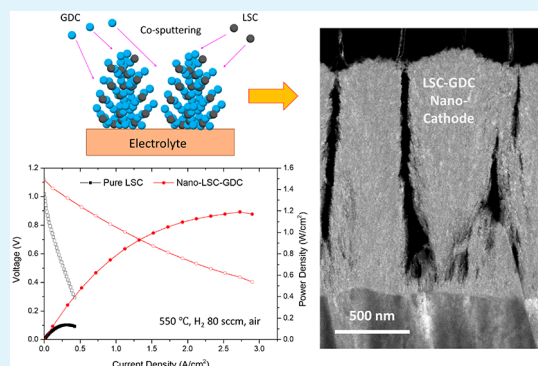
INTRODUCTION

Solid oxide fuel cells (SOFCs) are being considered and developed for a variety of power generation uses, ranging from watt- to megawatt-sized power systems.[1] Current SOFCs typically operate between 650 and 950 °C. High operating temperatures present several technical challenges, such as a more limited materials selection, an increased chance of undesirable chemical interactions between the cell components, and other operational restrictions (e.g., slow startup and thermal cycling). To mitigate these issues, it is desirable to lower the operating temperature of SOFCs while maintaining high performance. Since the conductivity of the electrolyte largely determines the fuel cell operating temperature, reducing the electrolyte thickness by fabricating thin-film SOFCs (TF-SOFCs) is one avenue toward lowering the operating temperature. There are several different approaches that have been evaluated for fabricating TF-SOFCs: chemical vapor deposition (CVD) techniques such as aerosol-assisted CVD (AACVD),[2,3] metal−organic CVD (MOCVD),[4] atomic layer deposition (ALD),[5,6] or physical vapor deposition (PVD) techniques such as electron beam PVD (EB-PVD),[7,8] pulsed laser deposition (PLD),[9−11] and sputtering.[12−14]

Among the various TF-SOFC PVD fabrication methods, magnetron sputtering allows for better control of the morphology of the deposited thin films (whether it is a dense electrolyte or porous electrodes) by modifying the sputtering conditions. Apart from that, magnetron sputtering has the advantage of room-temperature deposition and has the potential for large-area deposition, enabling fabrication scale-up. Fabrication of TF-SOFCs with magnetron-sputtered yttria-stabilized zirconia (YSZ) has been previously demonstrated.[14,15] By adjusting the sputtering pressure, target-to-sample distance, and sputtering power, the energy and direction of the sputtered materials can be controlled, allowing the nanostructure of the deposited layers to be tuned.[16] As for the cathode, sputtered metallic porous cathodes such as Pt and Ag are commonly used for low-temperature (<500 °C) operation in TF-SOFCs, but these tend to degrade after long-term
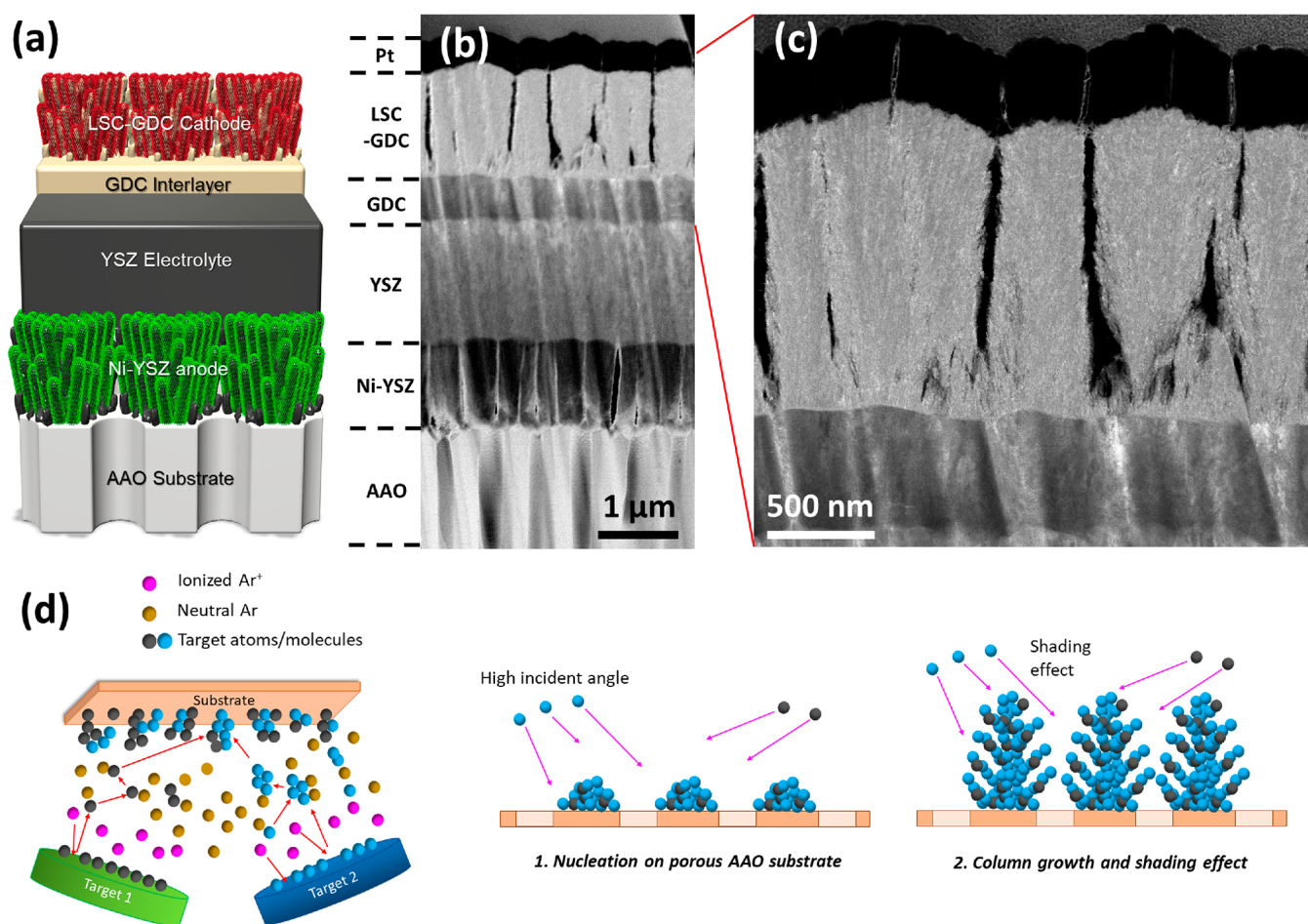
Figure 1. (a) Configuration of TF-SOFC. (b) Dark field cross-sectional STEM image of the sputtered TF-SOFC. (c) Dark field cross-sectional STEM image of the nano-ceramic cathode. (d) Schematic of the co-sputtering process and the deposited nano-ceramic cathode nanostructure and column growth process.

operation at higher temperatures (500−700 °C) due to severe metal agglomeration that irreversibly destroys the nanostructure of the cathode.[17−19] To improve thermal stability and maintain catalytic activity at high temperatures, ceramic mixed ionic and electronic conducting (MIEC) perovskite cathodes are commonly used.[20] Direct sputtering of ceramic materials usually results in dense films (independent of sputtering conditions) owing to the amorphous state in the as-deposited film. In previous studies of dense MIEC cathodes,[21−24] the ultrathin and dense cathode degraded over time and further increasing the thickness of the cathode did not improve the performance or stability. It is therefore beneficial to develop a sputtering process that can result in porous ceramic cathode films for TF-SOFCs. In previous works, there have been attempts to co-sputter or decorate noble metals with ceramics to form mixed cathodes.[25,26] However, the morphology of the nanostructure of the mixed cathode still changed over the course of operation, resulting in performance degradation.

In this work, we report the results of our study on YSZ-based TF-SOFCs with the lanthanum strontium cobaltite perovskite (LSC)-gadolinium-doped ceria (GDC) cathodes. Adding GDC into the MIEC perovskite to form a porous composite cathode greatly improves the performance by increasing the ionic conductivity of the perovskite cathode[27−29] and improves the stability by minimizing microstructural changes during operation. To combine the

advantages of sputtering metals and ceramic oxides, as noted in our previous work,[13] we conducted co-sputtering of a metal alloy target, $Gd_{0.2}Ce_{0.8}$ (Gd−Ce), with a ceramic LSC target, $(La_{0.6}Sr_{0.4})_{0.98}CoO_3$. Figure 1c shows transmission electron microscopy images (TEM, in scanning mode) of a co-sputtered nanostructured ceramic cathode. From the image, we can observe two distinctive porous features: one being columnar structures with large openings between each structure and the other being 10 nm diameter nanofibers which grow a branch-like nanostructure on a large columnar structure; such columnar structures have been observed previously and are caused by shadowing effects during deposition.[10,30,31] The nanofiber-like columnar nanostructure is an ideal structure for the cathode of TF-SOFCs since the openings ensure sufficient oxygen mass transport while the nanosized structure increases the effective active area. Furthermore, the co-sputtered GDC enhances mixed conductivity of the cathode, creating more triple-phase boundaries (TPBs) for the oxygen reduction reaction (ORR) process. The configuration of the full TF-SOFCs is illustrated in Figure 1a. The key to grow a nanoporous structure is to grow the sample in the zone 1 region of the Thornton diagram, or the so-called column growth region.[16] The growth mechanism, demonstrated in previous work,[13] is shown in Figure 1d. Porous anodized aluminum oxide (AAO) templates with a nanostructure of well-defined and uniform pores (100−250 nm) were
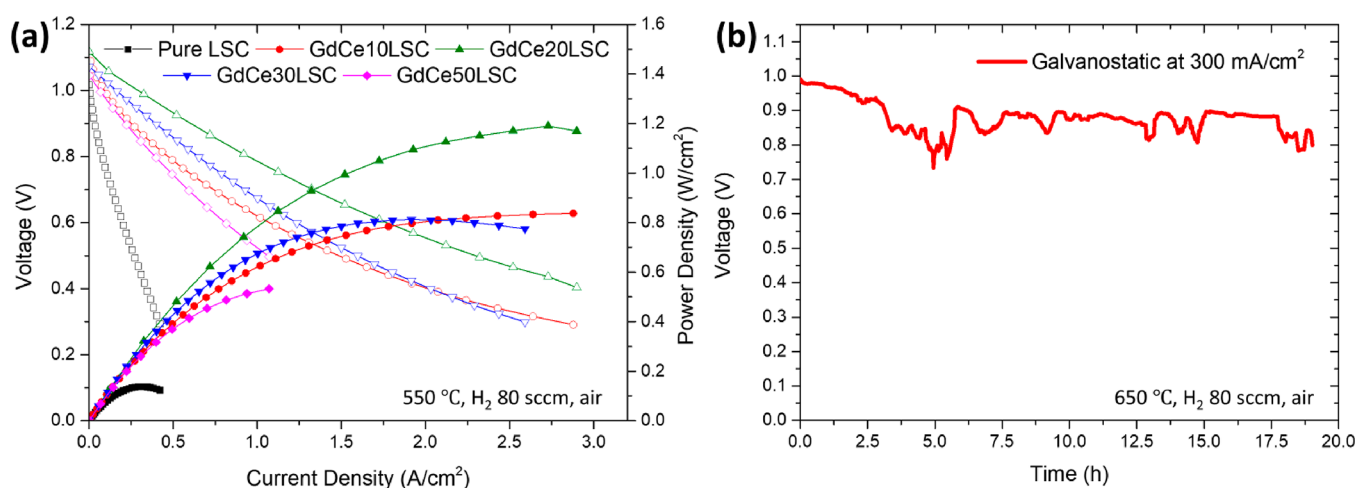
Figure 2. (a) Current density vs voltage and power density characteristics for LSC-GDC/GDC/YSZ/Ni-YSZ at 550 °C. (b) Durability test measured at 650 °C at a constant current density of 300 mA/cm^2.

used as the substrate. In previous works,[13,32,33] porous AAO templates have been shown to be a suitable substrate for TF-SOFCs. In our study, 100 μm thick AAO templates with a 120 nm pore size were used as the supporting substrate. For the anode, Ni and Y−Zr were co-sputtered to form a 900 nm thick porous anode nanostructure. For the electrolyte, YSZ was used. To avoid potential chemical reactions between the perovskite cathode and YSZ electrolyte and reduce the interfacial transport loss, dense and thin GDC was used as an interlayer between the cathode and YSZ electrolyte.[34−36] The thicknesses for the GDC and YSZ layers were 500 and 1900 nm, respectively. For the cathode, a porous ceramic LSC-GDC cathode was deposited on the GDC by co-sputtering with a thickness around 800−1000 nm. A 300 nm thick Pt layer was deposited on the cathode as a current collector. The detailed experimental methods are given in Section 10 in the Supporting Information. The STEM image for the full cell is shown in Figure 1b, which shows the nanostructure for each layer schematically depicted in Figure 1a. Energy-dispersive X-ray spectroscopy (EDX) mappings conducted on the sputtered cathode and anode (shown in Supporting Information Figure S1), generally indicate the correct distribution of the different elements. The signal intensities for different elements are consistent with the ratio of each element.

To systematically study the effects of the deposited cathode nanostructure and composition over the performance of TF-SOFCs, a series of cells with different cathode compositions were fabricated via controlling the sputtering conditions. The cathodes were co-sputtered by using a constant power of 200 W for the LSC target and varying the power of the Gd−Ce alloy target (0, 10, 20, 30, and 50 W). The cathodes are denoted as pure LSC, GdCe10LSC, GdCe20LSC, GdCe30LSC, and GdCe50LSC, respectively. The active area in our cells is 1 mm^2, and the configuration of the cell and the test setup are provided in Figure S2 of the Supporting Information. Potentiostatic, galvanostatic, and power polarization modes for the Gamry Reference 3000 were used to measure the electrochemical properties of the fabricated TF-SOFCs. To minimize damage from high current densities and overpotentials, the measurements limited the maximum current density and minimum voltage to 7 A/cm^2 and 0.3 V, respectively. The current density−voltage ($I−V$) curves and power density (PD)−current density curves (measured at 550

°C) are shown in Figure 2a for the different sputtered cells. Measurements conducted at 450, 500, 600, and 650 °C are shown in Figure S3. It was observed that the PD at 600 and 650 °C increased with increasing current density without showing a peak at high current densities. This was most likely a result of the cell heating up due to the high current density. This only happens when current density rises above a certain threshold due to the limitation of heat dissipation in small cells. The peak PD at these temperatures was thus determined by fitting the power density data at lower current densities to a parabolic curve; the methodology is shown in Figure S4.

Table 1 summarizes the open-circuit voltages (OCVs) and peak PDs measured at different temperatures for the sputtered

Table 1. Summary of the OCV and Peak Power Density at Various Temperature for Cells with Different LSC-GDC Cathodes

temp	OCV (V)	peak PD (W/cm^2)				
	500 °C	450 °C	500 °C	550 °C	600 °C	650 °C
pure LSC	1.02	0.01	0.07	0.14	0.23	0.23
GdCe10LSC	1.10	0.08	0.26	0.83	1.86	2.31
GdCe20LSC	1.12	0.14	0.48	1.19	2.56	3.01
GdCe30LSC	1.10	0.12	0.32	0.81	2.16	3.37
GdCe50LSC	1.08	0.04	0.17	0.53	0.81	1.68

cells. All of the OCV values are close to the theoretical values. The OCV of a commercial cell mounted on the same test station was about 1.06 V, similar to our TF-SOFC cells, indicating insignificant gas cross-leakage and proper sealing for the measurement setup. Compared to the pure LSC cathode (dense), the co-sputtered, porous cathodes show significantly higher power densities at all of the measured temperatures. Among the samples, GdCe20LSC shows the best performance, with peak PDs of 0.14, 0.48, 1.19, 2.56, and 3.01 W/cm^2 obtained at 450, 500, 550, 600, and 650 °C, respectively, the highest PD values that have been observed for YSZ-based TF-SOFCs.

To test reproducibility, multiple GdCe20LSC samples (5 in total) were tested at 550 and 600 °C and the error bars were obtained and shown in Figure S5. It can be seen from Figure S5 that in spite of some performance variation commonly observed in SOFC cell testing, the experimental data show
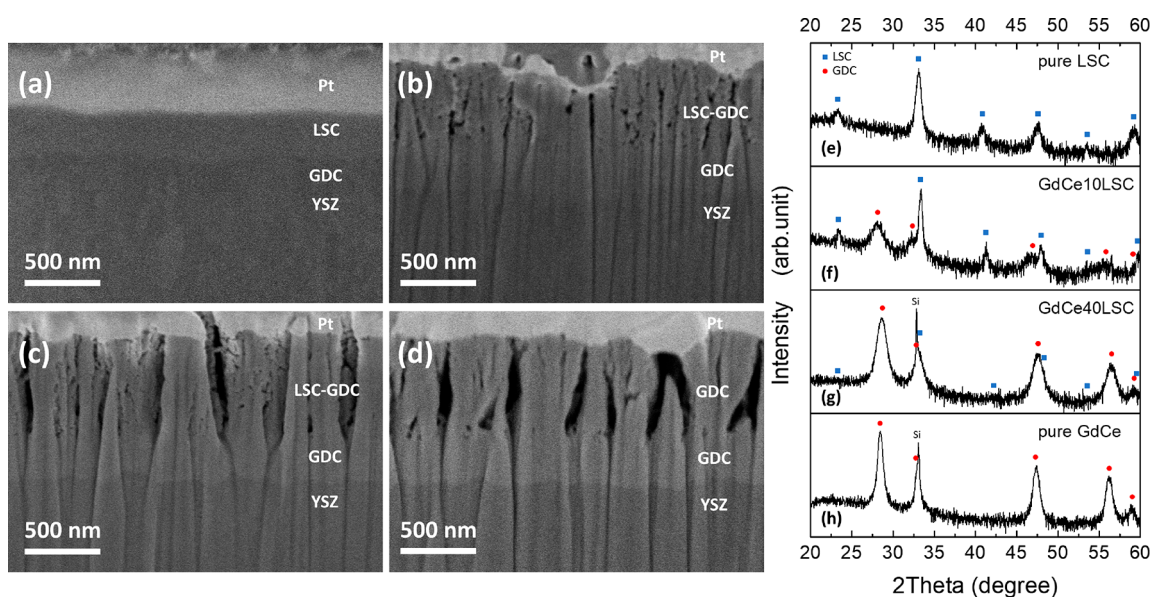
Figure 3. Cross-sectional SEM images and corresponding XRD patterns for (a and e) pure LSC cathode, (b and f) co-sputtered GdCe10LSC cathode, (c and g) co-sputtered GdCe40LSC cathode, and (d and h) pure GdCe cathode. Intensities are presented in log-scale.

consistent performance. Notably, the peak PD for GdCe20LSC is slightly lower than that for GdCe30LSC at 650 °C and a comparison of different power densities of SOFCs measured at several different temperatures are shown in Figure S6. Overall, this comparison shows the superior power density for TF-SOFC with the nano-ceramic LSC-GDC cathode.

For durability testing, a co-sputtered cell was operated at 650 °C under a current density of 300 mA/cm². The test results are shown in Figure 2b, indicating that the cell was relatively stable over 20 h; it decayed less than 15%.

To verify the scalability of our fabrication method, cells with an active area of 5 × 4 mm² were fabricated. The peak PD and IV curves are shown in Figure S7 and compared to the same cell configuration that had a 1 mm² active area. There is no significant discrepancy between the small cell and the larger cell, which indicates the validity of our transport measurement and the scalability of the sputtering method.

The cells were characterized using cross-sectional SEM images, and X-ray diffraction (XRD) patterns were obtained for each different cathode. The SEM images are shown in Figure 3a–d for pure LSC, GdCe10LSC, GdCe40LSC, and Pure GdCe. SEM images of the tested cell are also included in Figure S8. There is insignificant change of morphology before and after testing. From these images, there is a clear transition from a completely dense structure (pure LSC) to a porous structure once co-sputtering of LSC with Gd–Ce was conducted. Using a higher sputtering power of the Gd–Ce target (a higher GDC content in the layer) resulted in a composite with a higher porosity and increased ionic conductivity. In principle, with higher porosity and increased ionic conductivity in electrodes, the PD will be higher due to a larger active surface area and a lower cathodic polarization resistance. This trend was observed experimentally; however, once the Gd–Ce power exceeded 20 W, the PD decreased. This phenomenon indicates that the cathode composition, not just the morphology, also plays an important role.

To understand structural effects from the compositional changes of the co-sputtered cathode, the same cathodes

previously mentioned were sputtered on Si/SiO₂ wafers and annealed at the typical operation temperature (600 °C) for 2 h before being measured by XRD. The resulting XRD patterns are shown in Figure 3e–h, and the peaks for LSC and GDC are labeled with blue squares and red circles, respectively. The sharp peak at $2\theta = 33°$ corresponds to the Si(200) peak from the Si/SiO₂ substrate. The XRD pattern in Figure 3e corresponds to the sputtered pure dense LSC cathode as shown in the SEM image in Figure 3a; this XRD pattern only shows the peaks for LSC without any peaks from GDC, as expected. With co-sputtering of LSC with 10 W Gd–Ce, GDC peaks start to appear, while LSC peaks become less intense. As the sputtering power of GDC was gradually increased from 10 to 40 W, the GDC peaks become more prominent and the LSC peaks continue to decrease in intensity until virtually only the GDC peaks are seen (with pure Gd–Ce). Assuming the strain and stress in the thin films are negligible after annealing, by fitting the peak widths with the *Scherrer* equation, we obtain the crystallite size (coherence length) for each phase, which is a measure of the size of the nanoparticles. The extracted crystallite sizes for LSC are 105.8 nm (pure LSC) and 165.9 nm (GdCe10LSC), and the crystallite sizes for GDC are 52.4 nm (GdCe10LSC), 80.8 nm (GdCe40LSC), and 169 nm (pure GdCe); both increase proportionally to the GDC ratio. In general, the larger the crystallite size is, the smaller the TPB will be. This change of composition and crystallite size in the cathodes decreases the TPB length, resulting in lowered power densities. The characterization results seem to reinforce that the nanostructure and composition of the cathode are the two main factors that impact the performance in our TF-SOFCs. The two competing mechanisms appear to be as follows: (1) a higher Gd–Ce ratio will dramatically enhance the porosity and ionic conductivity of the mixed conductivity in the cathode, but (2) a lower ratio of LSC will yield a shorter TPB length in the cathode and decrease catalytic activity. Among all of the fabricated cathodes, the peak performance was obtained when co-sputtering the Gd–Ce target at a power of 20 W. Compared to the sample after annealing (similar conditions as after testing), the as-deposited sample shows a similar XRD
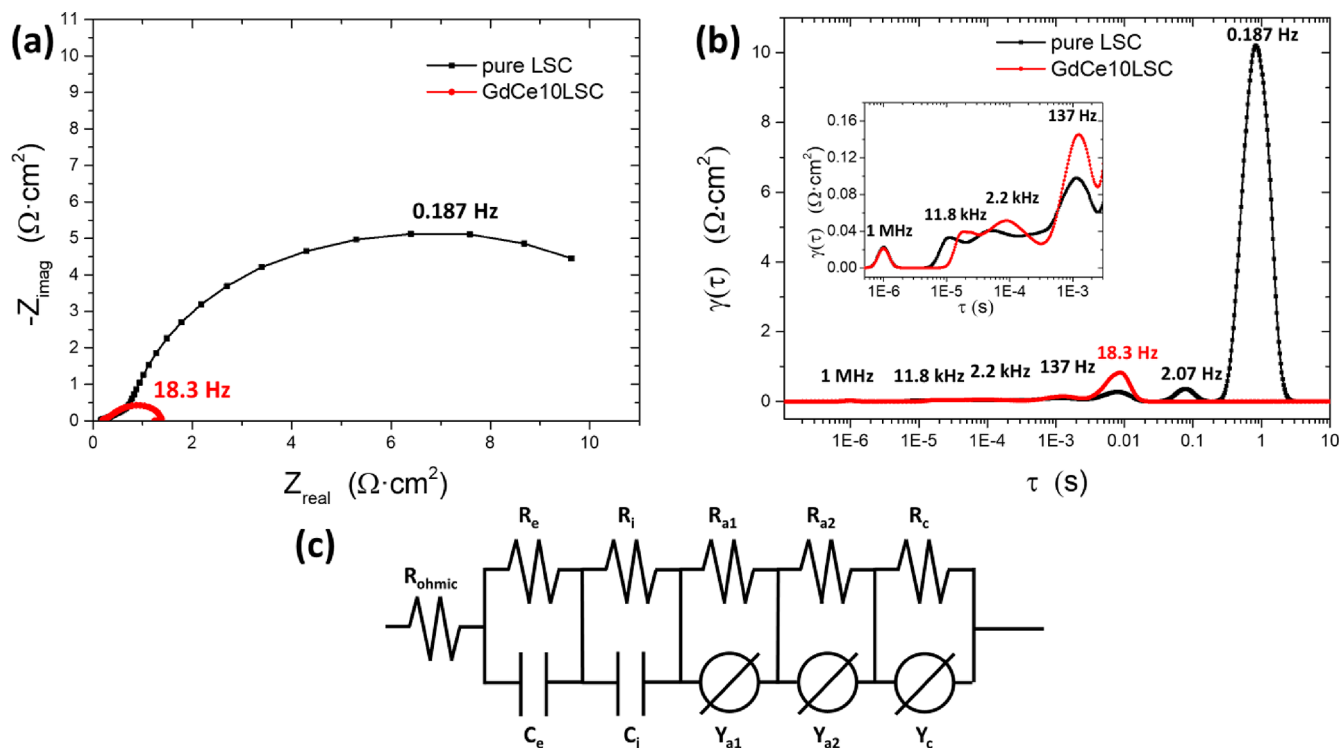
Figure 4. (a) EIS for pure LSC (black), co-sputtered GdCe10LSC cathode (red) and (b) the corresponding data transformed into DFRT curves. (c) Equivalent circuit used for the EIS fitting.

pattern but with less-intense LSC peaks. We believe this is due to grain growth of the LSC phase and thus an increase in the crystallinity of LSC during the annealing process.

Electrochemical impedance spectroscopy (EIS) was conducted during cell operation. To get quantitatively reliable data for cathode and anode separately, the distributed function of relaxation time (DFRT) method was conducted on the EIS data. DFRT characterization of EIS data is a convenient method to distinguish the different impedance contributions in TF-SOFCs.[37] DFRT transforms EIS data from the frequency domain to the time domain to distinguish contributions from different processes more clearly. In general, these processes are made up of a series of reaction steps: (i) adsorption of electroactive gaseous species (hydrogen or oxygen), (ii) dissociation of electroactive species on the electrode surface, (iii) diffusion of adsorbed species on the electrode surface to TPB sites, (iv) diffusion of oxygen ions to/from TPBs, and (v) charge transfer reactions. To investigate the high performance in our sputtered cathodes, galvanostatic EIS and DFRT were conducted for pure LSC cathode and co-sputtered GdCe10LSC cathode at 550 °C and the data are shown in Figure 4a,b. The AC frequency range was from 1 MHz to 0.1 Hz, and the impedance was measured at OCV. The DRT tool software was used to transform EIS data into the time domain for analysis,[38,39] and a Gaussian distribution was used in the fitting. As shown in the EIS data in Figure 4a, the Ohmic resistances in two samples are close to each other, indicating the YSZ electrolyte and GDC interlayer are properly deposited. The small difference in each sample might be from variations in the Ohmic resistance of the electrolyte. From the DFRT data in Figure 4b, 5 main peaks were observed, located at 1 MHz (P_e), 14.0−11.8 kHz (P_i), 3.2−2.2 kHz (P_{a1}), 137−136 Hz (P_{a2}), and 18.3−0.187 Hz ($P_{c1} + P_{c2} = P_c$). Here P_{c1} and P_{c2} can be treated as a combined P_c since the

gas diffusion, adsorption, and charge transfer reaction are coupled (and difficult to deconvolute) in MIEC cathodes.

The polarization resistances for each peak vary for each sample. To separate the polarization loss from the anode and cathode, different temperatures and hydrogen partial pressures were applied by mixing helium gas to the anode. The DFRT figures for different hydrogen partial pressures and temperature measured for pure LSC cathode are plotted in Figure 5a,b. From the DFRT figures, the two peaks around 3.2−2.2 kHz (P_{a1}) and 137−136 Hz (P_{a2}) come from the anode (since it changes with the hydrogen partial pressure) while the other three peaks are independent of the hydrogen partial pressure. These two peaks can be described by a constant phase element (CPE) in parallel with resistor (R), denoted as CPE//R. The two peaks above 1 MHz (P_e) and around 14.0−11.8 kHz (P_i) only change with temperature, and their frequencies increase with increasing temperature as shown in Figure 5c,d, so we assume that these come from the ionic transport process in the bulk electrolytes and the interface polarization resistance between electrolyte and anode; these two contributions are defined using a resistor in parallel with pure capacitance (C) denoted as R//C. The peaks at the lowest frequency from 18.3 to 0.187 Hz (P_c) are independent of the hydrogen partial pressure but dramatically change with the different cathodes. This can come from the surface exchange process and ionic and charge transport processes in the cathode. This peak could not be simply described by a R//C component as shown in Figure 4a, since the cathode is a typical MIEC which therefore does not behave like a pure double layer capacitor due to the bulk oxygen diffusion.[40,41] Here we use the CPE//R component to represent this composite cathode.[42] The equivalent circuits are shown in Figure 4c, and the fitting parameters and results are listed in Tables S1 and S2. The equivalent capacitance C values for all CPE//R components
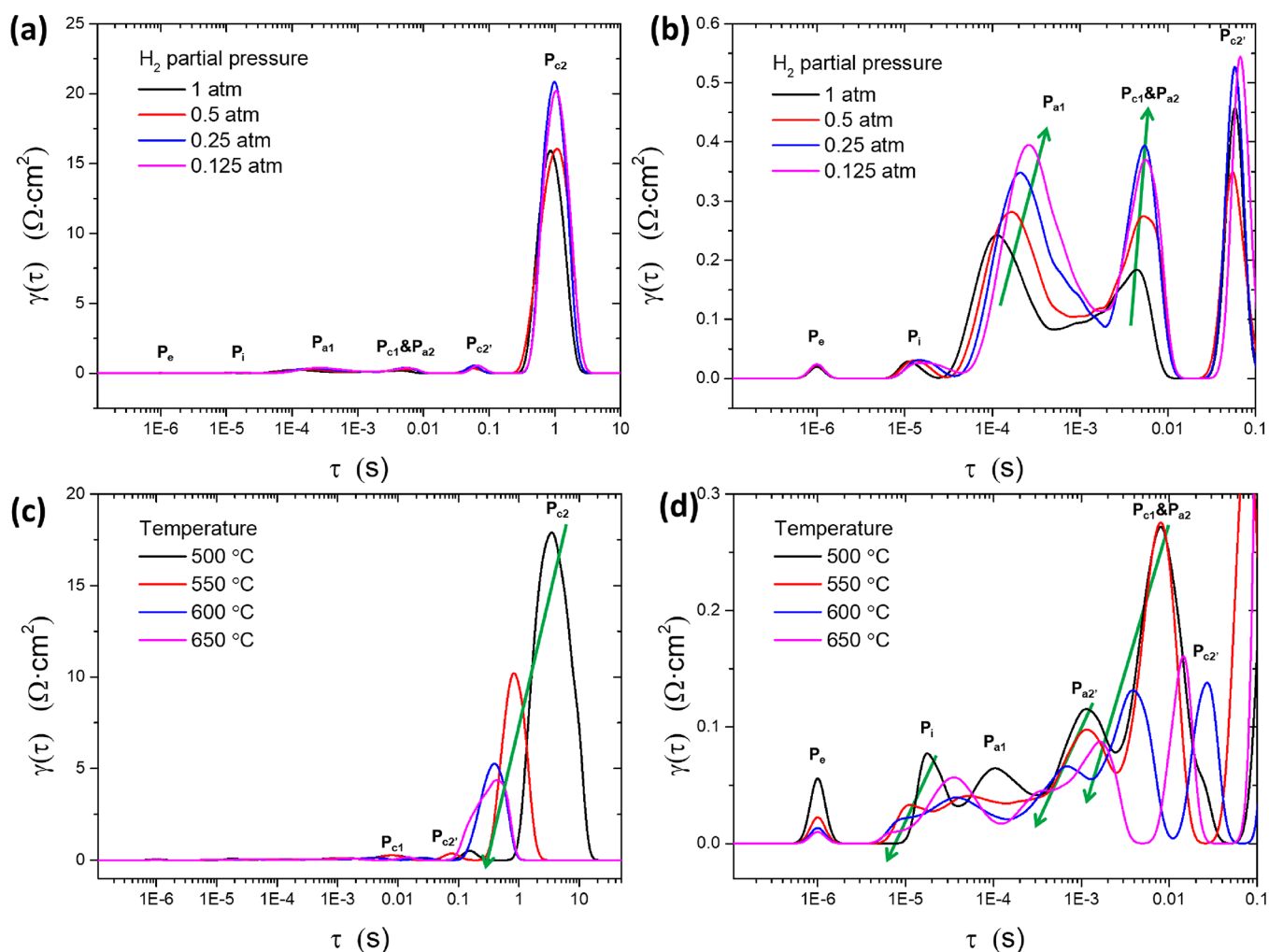
Figure 5. DFRT analysis for the pure LSC cathode: (a) overall and (b) zoomed-in view of the DFRT influenced by different hydrogen partial pressures and (c) overall and (d) zoomed-in view of DFRT influenced by different temperatures.

are effective capacitances calculated from the fitting parameters Q and n of the CPE component through the equation $C = (R^{1-n}Q)^{1/n}$, where R is the resistance of the parallel resistor, Q is the value of the admittance, and n is a constant. It is clearly seen that P_e, P_i, P_{a1}, and P_{a2} in different cells are close to each other since these have an identical anode and electrolyte. The only difference in the EIS fitting data comes from the cathode P_c, intuitive since that was the component that was varied. The fitted cathodic polarization resistance R_c for pure LSC and co-sputtered GdCe10LSC cathode are 11.15 and 0.56 $\Omega\cdot cm^2$, respectively. The two-order decrease of cathodic polarization resistance for the co-sputtered composite cathode results from the increased porosity and better ionic conductivity in the composite cathode, which in turn was caused by the superior porous nanostructure and with the introduction of GDC in the cathode. Table 2 summarizes the various reaction steps assigned from the DFRT data analysis.

■ CONCLUSION

In summary, nano-ceramic cathodes for TF-SOFCs were fabricated by co-sputtering a Gd−Ce alloy with LSC. Cells containing these composite cathodes showed superior power density at low temperatures, from 0.14 W/cm^2 at 450 °C to 3.01 W/cm^2 at 650 °C. Characterizations by TEM, SEM, XRD, and electrochemical measurements show that the

Table 2. Assigned Reaction Steps for the DFRT Data Analysis

DFRT peak	frequency	reacn step assigned
P_e	above 1 MHz	diffusion of oxygen ions in the electrolyte to TPB
P_i	14.0−11.8 kHz	transfer of oxygen ions from the bulk electrolyte to TPB sites
P_{a1}	3.2−2.2 kHz	hydrogen adsorption, dissociation, and diffusion of adsorbed hydrogen atoms to anode TPB sites
P_{a2}	137−136 Hz	charge transfer reaction between oxygen ions and adsorbed hydrogen atoms at TPB sites
P_c	18.3−0.187 Hz	oxygen adsorption, dissociation, diffusion of adsorbed oxygen atoms to cathode TPB sites and charge transfer reaction of adsorbed oxygen atoms

composition and nanostructure of the cathode are the two main factors that impact the power density of the TF-SOFCs. By comparing the EIS data of the deposited pure LSC cathode with co-sputtered composite cathodes, it can be seen the cathodic polarization resistance of the composite cathode dramatically decreased due to the superior nanostructure and optimized ratio of LSC to Gd−Ce. The peak power densities observed for sputtered thin-film cells are the highest among YSZ-based TF-SOFCs in the temperature range of 450−650

°C. This method of fabricating nanostructured ceramic composite cathodes by co-sputtering has been successfully demonstrated with Gd−Ce and LSC. The reproducibility and scalability of the magnetron sputtering platform have been illustrated in this letter and can thus be further adapted, namely, in using a variety of other materials, or for increasing the active area, to make TF-SOFCs for practical applications.

■ ASSOCIATED CONTENT

Ⓢ Supporting Information

The Supporting Information is available free of charge at https://pubs.acs.org/doi/10.1021/acsaem.0c01147.

Cell configuration and test setup, power density at different temperatures, fitted peak power density, reproducibility test, comparison of cell performance, scalability test, EDX and EIS fitting parameters, and detailed experimental methods (PDF)

■ AUTHOR INFORMATION

Corresponding Author

Nguyen Q. Minh − Center for Energy Research, University of California, San Diego, La Jolla, California 92093, United States; ⓘ orcid.org/0000-0003-3276-6150; Email: nminh@ucsd.edu

Authors

Haowen Ren − Materials Science and Engineering and Center for Memory and Recording Research, University of California, San Diego, La Jolla, California 92093, United States; ⓘ orcid.org/0000-0001-9343-5369

Yoon Ho Lee − Center for Energy Research, University of California, San Diego, La Jolla, California 92093, United States; School of Mechanical Engineering, University of Ulsan, Ulsan 44610, Republic of Korea

Erik A. Wu − Department of Nanoengineering, University of California, San Diego, La Jolla, California 92093, United States

Hyeseung Chung − Department of Nanoengineering, University of California, San Diego, La Jolla, California 92093, United States

Ying Shirley Meng − Department of Nanoengineering, Center for Memory and Recording Research, and Sustainable Power and Energy Center (SPEC), University of California, San Diego, La Jolla, California 92093, United States; ⓘ orcid.org/0000-0001-8936-8845

Eric E. Fullerton − Materials Science and Engineering, Department of Nanoengineering, Center for Memory and Recording Research, Sustainable Power and Energy Center (SPEC), and Department of Electrical and Computer Engineering, University of California, San Diego, La Jolla, California 92093, United States

Complete contact information is available at:
https://pubs.acs.org/10.1021/acsaem.0c01147

Notes

The authors declare no competing financial interest.

■ ACKNOWLEDGMENTS

■ REFERENCES

(1) Minh, N. Q. Solid Oxide Fuel Cell Technology — Features and Applications. *Solid State Ionics* **2004**, *174*, 271−277.

(2) Jang, D. Y.; Han, G. D.; Choi, H. R.; Kim, M. S.; Choi, H. J.; Shim, J. H. $La_{0.6}Sr_{0.4}Co_{0.2}Fe_{0.8}O_{3-\delta}$ Cathode Surface-Treated with $La_2NiO_{4+\delta}$ by Aerosol-Assisted Chemical Vapor Deposition for High Performance Solid Oxide Fuel Cells. *Ceram. Int.* **2019**, *45* (9), 12366−12371.

(3) Kim, J. W.; Jang, D. Y.; Kim, M.; Choi, H. J.; Shim, J. H. Nano-Granulization of Gadolinia-Doped Ceria Electrolyte Surface by Aerosol-Assisted Chemical Vapor Deposition for Low-Temperature Solid Oxide Fuel Cells. *J. Power Sources* **2016**, *301*, 72−77.

(4) Gadea, C.; Hanniet, Q.; Lesch, A.; Marani, D.; Jensen, S. H.; Esposito, V. Aqueous Metal−Organic Solutions for YSZ Thin Film Inkjet Deposition. *J. Mater. Chem. C* **2017**, *5*, 6021−6029.

(5) An, J.; Kim, Y. B.; Park, J.; Gür, T. M.; Prinz, F. B. Three-Dimensional Nanostructured Bilayer Solid Oxide Fuel Cell with 1.3 W/cm^2 at 450°C. *Nano Lett.* **2013**, *13*, 4551−4555.

(6) Ji, S.; Cho, G. Y.; Yu, W.; Su, P. C.; Lee, M. H.; Cha, S. W. Plasma-Enhanced Atomic Layer Deposition of Nanoscale Yttria-Stabilized Zirconia Electrolyte for Solid Oxide Fuel Cells with Porous Substrate. *ACS Appl. Mater. Interfaces* **2015**, *7* (5), 2998−3002.

(7) Tanhaei, M.; Mozammel, M. Yttria-Stabilized Zirconia Thin Film Electrolyte Deposited by EB-PVD on Porous Anode Support for SOFC Applications. *Ceram. Int.* **2017**, *43* (3), 3035−3042.

(8) Han, F.; Sata, N.; Riegraf, M.; Fuchs, F. M.; Semerad, R.; Geipel, C.; Walter, C.; Costa, R. Thin-Film Gd-Doped Ceria Sr-Barrier Layers for Electrolyte Supported SOFCs. *ECS Trans.* **2019**, *91* (1), 1157−1163.

(9) Kwon, C.-W.; Son, J.-W.; Lee, J.-H.; Kim, H.-M.; Lee, H.-W.; Kim, K.-B. High-Performance Micro-Solid Oxide Fuel Cells Fabricated on Nanoporous Anodic Aluminum Oxide Templates. *Adv. Funct. Mater.* **2011**, *21*, 1154−1159.

(10) Kang, B. S.; Matsuda, J.; Ju, Y. W.; Kim, H. H.; Ishihara, T. Nano Strain Induced Double Columnar Oxide as Highly Active Oxygen-Dissociation Electrode for Ni-Fe Metal Supported Solid Oxide Fuel Cells. *Nano Energy* **2019**, *56*, 382−390.

(11) Zheng, Y.; Li, Y.; Wu, T.; Zhang, W.; Zhu, J.; Li, Z.; Chen, J.; Yu, B.; Wang, J.; Zhang, J. Oxygen Reduction Kinetic Enhancements of Intermediate-Temperature SOFC Cathodes with Novel $Nd_{0.5}Sr_{0.5}CoO_{3-\delta}/Nd_{0.8}Sr_{1.2}CoO_{4\pm\delta}$ Heterointerfaces. *Nano Energy* **2018**, *51* (May), 711−720.

(12) Barnett, S. A. A New Solid Oxide Fuel Cell Design on Thin Film Electrolytes. *Energy* **1990**, *15*, 1−9.

(13) Lee, Y. H.; Ren, H.; Wu, E. A.; Fullerton, E. E.; Meng, Y. S.; Minh, N. Q. All-Sputtered, Superior Power Density Thin-Film Solid Oxide Fuel Cells with a Novel Nanofibrous Ceramic Cathode. *Nano Lett.* **2020**, *20*, 2943−2949.

(14) Fondard, J.; Bertrand, P.; Billard, A.; Fourcade, S.; Batocchi, P.; Mauvy, F.; Bertrand, G.; Briois, P. Manufacturing and Testing of a Metal Supported Ni-YSZ/YSZ/La_2NiO_4 IT- SOFC Synthesized by Physical Surface Deposition Processes. *Solid State Ionics* **2017**, *310*, 10−23.

(15) Solovyev, A. A.; Shipilova, A. V.; Ionov, I. V.; Kovalchuk, A. N.; Rabotkin, S. V.; Oskirko, V. O. Magnetron-Sputtered YSZ and CGO Electrolytes for SOFC. *J. Electron. Mater.* **2016**, *45* (8), 3921−3928.

(16) Thornton, J. A. The Microstructure of Sputter-Deposited Coatings. *J. Vac. Sci. Technol., A* **1986**, *4*, 3059−3065.

(17) Wang, X.; Huang, H.; Holme, T.; Tian, X.; Prinz, F. B. Thermal Stabilities of Nanoporous Metallic Electrodes at Elevated Temperatures. *J. Power Sources* **2008**, *175*, 75−81.

(18) Chang, I.; Woo, S.; Lee, M.-H.; Shim, J.-H.; Piao, Y.; Cha, S.-W. Applied Surface Science Characterization of Porous Pt Films Deposited via Sputtering. *Appl. Surf. Sci.* **2013**, *282*, 463−466.

(19) Lee, Y.-H.; Cho, G.-Y.; Chang, I.; Ji, S.; Kim, Y.-B.; Cha, S.-W. Platinum-Based Nanocomposite Electrodes for Low-Temperature Solid Oxide Fuel Cells with Extended Lifetime. *J. Power Sources* **2016**, *307*, 289−296.

(20) O'Hayre, R.; Cha, S.-W.; Whitney, C.; Prinz, F. B. *Fuel Cell Fundamentals*, 1st ed.; Wiley, 2008.

(21) Lai, B.-K.; Johnson, A. C.; Xiong, H.; Ramanathan, S. Ultra-Thin Nanocrystalline Lanthanum Strontium Cobalt Ferrite ($La_{0.6}Sr_{0.4}Co_{0.8}Fe_{0.2}O_{3-1}$) Films Synthesis by RF-Sputtering and Temperature-Dependent Conductivity Studies. *J. Power Sources* **2009**, *186*, 115−122.

(22) Holme, T. P.; Lee, C.; Prinz, F. B. Atomic Layer Deposition of LSM Cathodes for Solid Oxide Fuel Cells. *Solid State Ionics* **2008**, *179*, 1540−1544.

(23) la O', G. J.; Shao-Horn, Y. Thickness Dependence of Oxygen Reduction Reaction Kinetics on Strontium-Substituted Lanthanum Manganese Perovskite Thin-Film Microelectrodes. *Electrochem. Solid-State Lett.* **2009**, *12* (5), B82−B85.

(24) la O', G. J.; Ahn, S.; Crumlin, E.; Orikasa, Y.; Biegalski, M. D.; Christen, H. M.; Shao-Horn, Y. Catalytic Activity Enhancement for Oxygen Reduction on Epitaxial Perovskite Thin Films for Solid-Oxide Fuel Cells. *Angew. Chem., Int. Ed.* **2010**, *49*, 5344−5347.

(25) Choi, H. J.; Kim, M.; Neoh, K. C.; Jang, D. Y.; Kim, H. J.; Shin, J. M.; Kim, G.-T.; Shim, J. H. High-Performance Silver Cathode Surface Treated with Scandia-Stabilized Zirconia Nanoparticles for Intermediate Temperature Solid Oxide Fuel Cells. *Adv. Energy Matter.* **2017**, *7*, 1601956.

(26) Muranaka, M.; Sasaki, K.; Suzuki, A.; Terai, T. The Effect of LSGM Nanoparticle Dispersion in Ag-LSGM Composite Thin-Film Cathode. *J. Electrochem. Soc.* **2008**, *155* (8), B860−B863.

(27) Murray, E. P.; Sever, M. J.; Barnett, S. A. Electrochemical Performance of $(La,Sr)(Co,Fe)O_3−(Ce,Gd)O_3$ Composite Cathodes. *Solid State Ionics* **2002**, *148*, 27−34.

(28) Myung, D.; Hwang, J.; Hong, J.; Lee, H.; Kim, B.-K.; Lee, J.-H.; Son, J.-W. Pulsed Laser Deposition of $La_{0.6}Sr_{0.4}CoO_{3-\delta}$-$Ce_{0.9}Gd_{0.1}O_{2-\delta}$ Nano-Composite and Its Application to Gradient-Structured Thin-Film Cathode of SOFC. *J. Electrochem. Soc.* **2011**, *158* (8), B1000−B1006.

(29) Benel, C.; Darbandi, A. J.; Djenadic, R.; Evans, A.; Tölke, R.; Prestat, M.; Hahn, H. Synthesis and Characterization of Nano-particulate $La_{0.6}Sr_{0.4}CoO_{3-\delta}$ Cathodes for Thin-Film Solid Oxide Fuel Cells. *J. Power Sources* **2013**, *229*, 258−264.

(30) Ju, Y.; Hyodo, J.; Inoishi, A.; Ida, S.; Tohei, T.; So, Y.-G.; Ikuhara, Y.; Ishihara, T. Double Columnar Structure with a Nanogradient Composite for Increased Oxygen Diffusivity and Reduction Activity. *Adv. Energy Mater.* **2014**, *4*, 1400783.

(31) Kang, S. B.; Inoishi, A.; Takagaki, A.; Ishihara, T. $Pr_2Ni_{0.71}Cu_{0.24}Ga_{0.05}O_4$-$Sm_{0.2}Ce_{0.8}O_{1.9}$ Composite Film as Active Cathodic Layer for Intermediate Temperature Solid Oxide Fuel Cells. *Solid State Ionics* **2018**, *327*, 59−63.

(32) Park, J.; Lee, Y.; Chang, I.; Lee, W.; Cha, S. W. Engineering of the Electrode Structure of Thin Film Solid Oxide Fuel Cells. *Thin Solid Films* **2015**, *584*, 125−129.

(33) Cho, G.-Y.; Lee, Y.-H.; Cha, S.-W. Multi-Component Nano-Composite Electrode for SOFCS via Thin Film Technique. *Renewable Energy* **2014**, *65*, 130−136.

(34) De Vero, J. C.; Develos-Bagarinao, K.; Kishimoto, H.; Ishiyama, T.; Yamaji, K.; Horita, T.; Yokokawa, H. Enhanced Stability of Solid Oxide Fuel Cells by Employing a Modified Cathode-Interlayer Interface with a Dense $La_{0.6}Sr_{0.4}Co_{0.2}Fe_{0.8}O_{3-\delta}$ Thin Film. *J. Power Sources* **2018**, *377*, 128−135.

(35) Wang, F.; Brito, M. E.; Yamaji, K.; Cho, D.-H.; Nishi, M.; Kishimoto, H.; Horita, T.; Yokokawa, H. Effect of Polarization on Sr and Zr Diffusion Behavior in LSCF/GDC/YSZ System. *Solid State Ionics* **2014**, *262*, 454−459.

(36) Park, T.; Lee, Y.-H.; Cho, G.-Y.; Ji, S.; Park, J.; Chang, I.; Cha, S.-W. Effect of the Thickness of Sputtered Gadolinia-Doped Ceria as a Cathodic Interlayer in Solid Oxide Fuel Cells. *Thin Solid Films* **2015**, *584*, 120−124.

(37) Boukamp, B. A.; Rolle, A. Use of a Distribution Function of Relaxation Times (DFRT) in Impedance Analysis of SOFC Electrodes. *Solid State Ionics* **2018**, *314*, 103−111.

(38) Wan, T. H.; Saccoccio, M.; Chen, C.; Ciucci, F. Influence of the Discretization Methods on the Distribution of Relaxation Times Deconvolution of Relaxation Times: Implementing Radial Basis Functions with DRTtools. *Electrochim. Acta* **2015**, *184*, 483−499.

(39) Saccoccio, M.; Wan, T.-H.; Chen, C.; Ciucci, F. Optimal Regularization in Distribution of Relaxation Times Applied to Electrochemical Impedance Spectroscopy: Ridge and Lasso Regression Methods - A Theoretical and Experimental Study. *Electrochim. Acta* **2014**, *147*, 470−482.

(40) Jørgensen, M. J.; Mogensen, M. Impedance of Solid Oxide Fuel Cell LSM/YSZ Composite Cathodes. *J. Electrochem. Soc.* **2001**, *148*, A433−A442.

(41) Baumann, F. S.; Fleig, J.; Cristiani, G.; Stuhlhofer, B.; Habermeier, H.; Maier, J. Quantitative Comparison of Mixed Conducting SOFC Cathode Materials by Means of Thin Film Model Electrodes. *J. Electrochem. Soc.* **2007**, *154*, B931−B941.

(42) Brug, G. J.; Van Den Eeden, A. L. G.; Sluyters-Rehbach, M.; Sluyters, J. H. The Analysis of Electrode Impedances Complicated by the Presence of a Constant Phase Element. *J. Electroanal. Chem. Interfacial Electrochem.* **1984**, *176*, 275−295.